RESEARCH ARTICLE

Key Points:
- Convergent radial transport is modeled in random anisotropic formations
- Apparent capacity coefficient follows the same anisotropic patterns of ln(K)
- This behavior is linked to transport connectivity and stratification

Supporting Information:
- Appendix B
- Figure S1
- Table 1

Correspondence to:
D. Pedretti,
dpedretti@eos.ubc.ca

Apparent directional mass-transfer capacity coefficients in three-dimensional anisotropic heterogeneous aquifers under radial convergent transport

D. Pedretti[1], D. Fernàndez-Garcia[2], X. Sanchez-Vila[2], D. Bolster[3], and D. A. Benson[4]

[1]Department of Earth, Ocean and Atmospheric Sciences, University of British Columbia, Vancouver, British Columbia, Canada, [2]Department of Geotechnical Engineering and Geo-Sciences, UPC-Barcelona Tech, Spain, [3]Department of Civil and Environmental Engineering and Earth Sciences, University of Notre Dame, South Bend, Indiana, USA, [4]Hydrologic Science and Engineering, Colorado School of Mines, Golden, Colorado, USA

Abstract Aquifer hydraulic properties such as hydraulic conductivity (K) are ubiquitously heterogeneous and typically only a statistical characterization can be sought. Additionally, statistical anisotropy at typical characterization scales is the rule. Thus, regardless of the processes governing solute transport at the local (pore) scale, transport becomes non-Fickian. Mass-transfer models provide an efficient tool that reproduces observed anomalous transport; in some cases though, these models lack predictability as model parameters cannot readily be connected to the physical properties of aquifers. In this study, we focus on a multirate mass-transfer model (MRMT), and in particular the apparent capacity coefficient (β), which is a strong indicator of the potential of immobile zones to capture moving solute. We aim to find if the choice of an apparent β can be phenomenologically related to measures of statistical anisotropy. We analyzed an ensemble of random simulations of three-dimensional log-transformed multi-Gaussian permeability fields with stationary anisotropic correlation under convergent flow conditions. It was found that apparent β also displays an anisotropic behavior, physically controlled by the aquifer directional connectivity, which in turn is controlled by the anisotropic correlation model. A high hydraulic connectivity results in large β values. These results provide new insights into the practical use of mass-transfer models for predictive purposes.

1. Introduction

Anisotropy and heterogeneity of hydraulic properties such as the hydraulic conductivity (K) are intrinsic to aquifers worldwide [e.g., *Rubin*, 2003]. Both features are linked to the geologic origin of aquifers and are not easily characterizable at the scales where solute transport typically occurs. A lack of detailed knowledge of the spatial distribution of hydraulic parameters at the local scale gives rise to uncertain spatiotemporal distributions of solute plumes, which has significant consequences for the prevention of groundwater pollution as well as the management and remediation of polluted aquifers [e.g., *Bolster et al.*, 2009; *de Barros et al.*, 2011].

Macroscopic anisotropy is a very well-known phenomenon in structural geology related to sedimentological processes, faulting and folding, and metamorphic processes. While in hydrogeology, it is common to refer to anisotropic formations as vertically axisymmetric media (e.g., stratified formations such as those present at the Grand Canyon, Colorado River, USA, depicted in Figure 1(bottom)), other forms of anisotropic formations also exist, such as those shown in Figure 1(top). Figure 1a depicts a conceptual sketch by *Koltermann and Gorelick* [1996] of oriented coarse-grained deposits embedded in a fine-grained matrix. The origin of these deposits is fluvial; well-connected coarse-grained structures appear to be distributed along one principle direction. Figure 1b corresponds to an outcrop of vertically oriented planes of fractures in a gneiss formation in Cordoba (Spain). The fractures originated from recent tectonic activities, and their orientation is collinear with the main stratification of the rock formation, tilted by an angle of 80–85° (i.e., subvertical). In this case, preferential flow paths along quasivertical planes are expected. It should be noted that the observation of anisotropy is scale dependent. An anisotropic description at the field scale gives no information as to whether or not the local behavior is isotropic.

Because it is infeasible to exhaustively model all local scale heterogeneous patterns affecting flow and solute transport dynamics, alternative (*effective*) models are powerful tools for capturing pertinent dynamics.
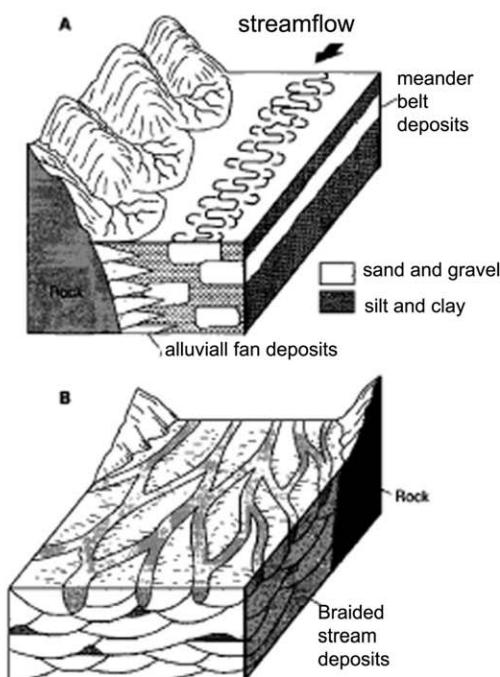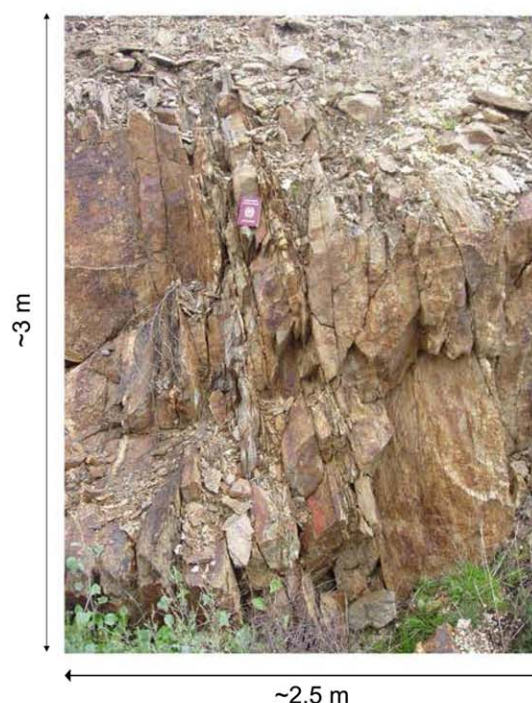
Figure 1. Three different anisotropic geological environments: (a) two conceptual sketches of a fluviatile sedimentation processes depending on the nature of the river (braided or meander) (from *Koltermann and Gorelick* [1996]). (b) An outcrop of a formation in Southern Spain showing subvertical fracturing and the potential of an axisymmetric anisotropy with a horizontal axis. (c) The Grand Canyon in the United States, characteristic of axisymmetric anisotropy with vertical axis.

These models aim to reproduce the average behavior of flow and solute plumes by means of upscaled (averaged) mathematical operators (such as macrodispersive terms) or using alternative mathematical models (such as nonlocal formulations) [e.g., *Rubin*, 2003]. In the context of (statistically) anisotropic porous media, effective models have been studied extensively since the early work on flow in perfectly stratified formations by *Gelhar et al.* [1979]. These authors were the first to derive values of directional effective *K* in randomly heterogeneous media. Later, many others developed a suite of solutions for expected values and

uncertainties (variances) for flow and solute concentrations in statistically anisotropic media under uniform flow conditions [see e.g., *Rubin*, 2003].

Significantly less work focuses on flow and transport under convergent (radial) flow conditions. *Sanchez-Vila and Carrera* [1997] showed that convergent flow tracer tests (CFTTs) in statistically nonisotropic media leads to variable directional travel times, which resulted in the concept of *apparent directional advective porosities*. It is important to note that CFTTs are sometimes preferable to uniform flow tracer tests in field applications for economic reasons [e.g., *Ptak et al.*, 2004]; additionally the analysis of convergent forced-gradient flow and solute transport problems is relevant in several practical circumstances such as delineation of well-capture zones or aquifer remediation using pump-and-treat activities.

Much previous work on upscaled transport in heterogeneous media departs from the assumption that conservative solutes in the subsurface can be perfectly modeled with an advection-dispersion equation (ADE). In recent years, this approach has been criticized due to its poor ability to properly reproduce field observations; observed BTCs from field experiments often display early arrivals, greater concentrations in late-time tails and highly nonsymmetric (skewed) distributions, while BTCs predicted by the ADE are generally symmetric (nonskewed). Nonsymmetric distributions of BTCs are also typically referred to as having *tailing*, and all these discrepancies between field observation and ADE predictions are lumped together under the general term *anomalous transport*. Among several causes that can explain the failure of the ADE, we highlight here the limited resolution and dimensionality of numerical models using the ADE, the assumption of multi-Gaussianity for ln K multivariate distributions, the lack of consideration of flow distributions other from uniform, and the assumption of ergodicity.

The dimensionality issue can be exemplified by the limited ability of two-dimensional (2-D) ADE-based numerical simulations to reproduce anomalous transport. 2-D numerical setups are largely adopted for practical reasons due to the lower computational burden compared with 3-D simulations. However, when used to simulate transport using the ADE model (especially assuming unconditional multi-Gaussian K fields), 2-D models offer a limited capacity to reproduce observed anomalous transport, leading to inaccurate identification of apparent transport parameters [*Sanchez-Vila et al.*, 1996]. Counterexamples are provided from 2-D simulations with very large ln K variance [e.g., *Le Borgne et al.*, 2008] or when inclusion models are used [e.g., *Fiori et al.*, 2006]. Tailing, however, has also been observed in experiments with low ln K variance and distributions of K different from embedded inclusions, such as in the 3-D laboratory experiments [e.g., *Fernàndez-Garcia et al.*, 2002] or field-scale tracer tests [e.g., *Riva et al.*, 2008]. A comparison between unconditional 2-D and 3-D multi-Gaussian numerical simulations by *Pedretti et al.* [2013] indicates that 2-D ADE-based simulations fail to reproduce tailing, while 3-D ADE-based simulations do produce such tailing, under convergent radial flow.

The inability of unconditional 2-D fields to generate anomalous transport may be related with the poor ability of 2-D configurations to reproduce important connectivity patterns that exist in typical aquifers. For example, some authors obtained anomalous distributions of BTCs from 2-D simulations after manipulating unconditional simulations to increase transport connectivity [e.g., *Zinn and Harvey*, 2003; *Willmann et al.*, 2008], thus effectively removing the idea of statistical stationarity from the system. These authors showed that connectivity not only affects the advection porosity, but also influences the choice of mass-transfer parameters in a theoretical formulation of transport based on overlapping mobile and immobile pore fractions (defined below). Interpretations of experiments by *Fernàndez-Garcia et al.* [2002] using a single porosity model show that anisotropy and connectivity are jointly two of the most important features controlling advection porosity in CFTTs. The issue of connectivity has been largely debated in recent years, although, to date, no unique quantifiable definition of connectivity exists [e.g., *Renard and Allard*, 2013].

Another complication relates to the injection-extraction distance (R) of CFTTs and the nonstationary flow that is typical in most experiments. As reported by *Gelhar* [1993], tracer tests are usually performed under highly nonergodic conditions, both because flow is radial in two-well settings and because R is often on the order of a few horizontal integral scales associated with the soil heterogeneity (I_x). However, for practical theoretical reasons [e.g., *Dagan*, 1989; *Rubin*, 2003] the tendency has been to build models of solute transport assuming ergodicity, which may not be a reasonable assumption as ergodicity can require an R on the order of tens to hundreds times I_x, even for uniform flow [*Matheron*, 1967].

In the recent paper by *Pedretti et al.* [2013], a set of 3-D unconditional multi-Gaussian numerical simulations of radial convergent transport in heterogeneous media showed that anomalous transport, displayed by

highly asymmetric depth-integrated BTCs, could be associated with transport stratification. This was particularly evident when R was on the order of I_x. The ratio between these two variables can be seen to largely impact not only the degree of asymmetry of the BTCs (i.e., the departure from ADE-predicted symmetric distributions, measured as the dimensionless time difference between the BTC concentration peak and its center of mass), but also the apparent power-law decrease of the BTC after the concentration peak. *Pedretti et al.* [2013] also indicate that the transverse dispersivity at the local scale (i.e., the Peclet number at the scale of a numerical grid cell) may have a small impact on the slope of apparent power-law tailing on the late-time BTCs and a stronger impact on the BTC's degree of asymmetry. However, in the latter case, an insufficient number of simulations were conducted to confidently evaluate the dependence of slope and degree of asymmetry with local dispersivity. A similar analysis on the influence of the flow velocity on the mass-transfer parameters was reported by *Sharifi Haddad et al.* [2012].

Both late-time power-law slopes and the degree of asymmetry are important indicators used for the inference of microscale heterogeneity using so-called *non-Fickian* or *nonlocal* models, a class of effective models which have emerged with the intent of better describing transport at intermediate to large scales. These methods include models based on multiporosity domains, which we focus on in this paper due to their wide use. Conceptually multiporosity models are based on the existence of heterogeneities at the microscopic level that exchange mass between fast (or mobile) aquifer zones and slower (or immobile) aquifer zones by mass transfer. One of these models, the multirate mass transfer (MRMT) model conceptualizes the aquifer as a multiporosity system made up of a continuum superposition of a mobile and multiple immobile domains [*Haggerty and Gorelick*, 1995; *Zinn and Harvey*, 2003]. Each immobile domain exchanges mass with the mobile domain at a different rate. The ratio of the sum of all immobile porosities and the mobile porosity defines a parameter called the *capacity coefficient* (β). This parameter controls the relative amount of mass that is present in the late-time BTC tail [*Pedretti et al.*, 2013]. The superposition of rates at which mass exchanges between these zones is described by a functional parameter called the *memory function* [*Carrera et al.*, 1998]. MRMT is also popular because chemical reactions can be readily incorporated [*Donado et al.*, 2009; *Willmann et al.*, 2010].

Mass-transfer models are widely used because of their versatility and ability to fit BTC tailing. However, mass transfer is a short name for a suite of complex physical processes linked to the existence of randomly distributed microscopic zones characterized by different pore-water velocities. Macroscopic evidence of mass-transfer processes includes heavily tailed BTCs observed during tracer tests; this phenomenological evidence has led some authors to postulate that heavily tailed BTCs may indicate the presence of mass-transfer processes at local scales. Nonetheless other processes can lead to tailing (e.g., advection in heterogeneous media) and can be confused with mass transfer. Additionally, a concrete relationship between the mathematical and aquifer physical parameters can be built only for a relatively limited number of cases, for instance when mass transfer is dominated by diffusion-like processes [*Nkedi-Kizza et al.*, 1984; *Haggerty and Gorelick*, 1995; *Carrera et al.*, 1998]. In this case, experimental evidence has validated this approach [e.g., *Gouze et al.*, 2008; *Zhang et al.*, 2007], and its use as a predictive tool is physically justifiable.

When tailing occurs in advection-dominated field experiments, a common situation widely observed in field and numerical experiments [e.g., *Becker and Shapiro*, 2000; *Zinn and Harvey*, 2003; *Fernàndez-Garcia et al.*, 2004; *Pedretti et al.*, 2013], mass-transfer-based formulations can be still used for fitting purposes but mass-transfer parameters become empirical, or *apparent* as they are not directly linked to any measurable physical property of the subsurface. This is generally why their validity as predictive tools is limited and why their use as effective upscaling approaches is highly criticized [e.g., *Neuman and Tartakovsky*, 2009]. Despite this, the possibility of generalizing non-Fickian model descriptions as practical predictive tools is highly appealing due to their relative simplicity. Several authors [e.g., *Zinn and Harvey*, 2003; *Willmann et al.*, 2008; *Flach*, 2012] have numerically explored phenomenological links between simulated aquifer properties and apparent parameters of non-Fickian upscaled models, but their general conclusion is that no unique solutions to fit model data exists. Experimental attempts to deal with this issue have also been documented [e.g., *Zinn et al.*, 2004], and while powerful due to methodological and technical limitations the results were somewhat unsatisfactory.

To date, it is generally not possible to establish a direct link between aquifer parameters and apparent mass-transfer parameters for advection-dominated problems. The aim of this paper is to show that it is possible to find a phenomenological correlation between the statistical anisotropic K distribution characterizing

heterogeneous porous media at intermediate scales and the anisotropic distribution of certain nonlocal parameters under a convergent flow scheme. We limit our paper to the analysis of the capacity coefficient β, which is a parameter based on the concept of mobile and immobile porosity; recall that porosities have been found to display directional properties in anisotropic aquifers [*Sanchez-Vila and Carrera*, 1997] under radial convergent flow.

Specifically, this paper aims to address the following two questions:

1. Does the apparent β depend upon anisotropy when estimated from CFTTs, as advection porosity does in single-porosity models?

2. What physical features control β?

Our approach is based on numerical models that solve for flow and transport in heterogeneous formations characterized by known anisotropic statistics, with a numerical setup similar to the one used by *Pedretti et al.* [2013]. The paper is structured as follows. In section 2, we develop our model and define the moment-based approach to find approximate estimates of β from the numerical BTCs. In section 3, we define important dimensionless variables. In section 4, we discuss statistical features controlling the value of β with discussion linking connectivity and β in section 5. Section 6 focuses on results from a single realization and conclusions are presented in section 7.

2. Directional and Anomalous Behavior of BTCs in Anisotropic Aquifers

2.1. Conceptual Model and Numerical Setup
Let us consider that CFTTs are performed in heterogeneous formations characterized by an oriented statistical distribution of the hydraulic conductivity, with similar patterns to the geological structures shown in Figure 1 (cases a and b). We assume that the tests are performed with ideal conservative tracers. A passive well (e.g., a piezometer) is used to inject the compounds and an active well, located at a planar distance (R), is used to capture the tracer over the time. We assume both wells to be fully screened along the entire vertical section of the aquifer, which has constant thickness (b). The active well pumps at a constant imposed rate (Q), until steady state flow conditions are attained before the tracer is injected. If R is small and Q is large, a typical natural background flow can be neglected and a purely convergent flow is assumed. The tracer test is performed by introducing a finite and known mass of solute (M) as a pulse input from the passive well, at a rate that does not affect the local groundwater level around it; we use a flux-averaged injection scheme [*Parker and Van Genuchten*, 1984]. The depth-integrated flux-averaged concentration is measured at the active well to obtain a breakthrough curve (BTC).

This conceptual setup can be modeled numerically following the methodology presented by *Pedretti et al.* [2013]. Full details regarding the numerical implementation of the log-transformed K fields, the numerical flow solution, and the evaluation of the BTC from a particle tracking algorithm are available therein. All fields are made up of a three-dimensional regular mesh of $251 \times 251 \times 100$ cubic cells of unit volume. The log-transformed hydraulic conductivity ($Y = \ln (K)$) values in each individual realization are drawn from a multi-Gaussian distribution with zero mean, finite variance $\sigma_Y^2 = 4$, and anisotropic exponential variograms. Within each cell Y is isotropic ($Y_x = Y_y = Y_z$), with the exception of the active well location at the center of the domain, where a vertical local K value five orders of magnitude larger than the mean value is imposed. A sink term is imposed at the bottom of the well, where the discharge rate is fixed. The use of high vertical local K in the cells corresponding to well position in the other layers simulates a fully penetrating well, without the need of imposing additional boundary conditions. Additional details can be found in *Pedretti et al.* [2013].

All simulations are carried out with a total constant porosity $\phi = 0.1$ and local dispersivity $a = 0.25$ (isotropic). These parameters control characteristic dimensionless numbers such as the Peclet numbers), which can influence on BTC shapes [e.g., *Riva et al.*, 2008] and/or on β [e.g., *Pedretti et al.*, 2013]. We do not present their specific influence in this context, as its qualitative influence can be understood from the results of cited papers. We leave detailed quantification open for future investigations.

To reproduce domains similar to those in Figure 1, we run stochastic simulations with different integral scales in the x, y, z directions (respectively, I_x, I_y, and I_z). Defining the anisotropy ratio between pairs of integer scales as $\epsilon_{ij} = I_i / I_j$, we focus on two sets of geometries:
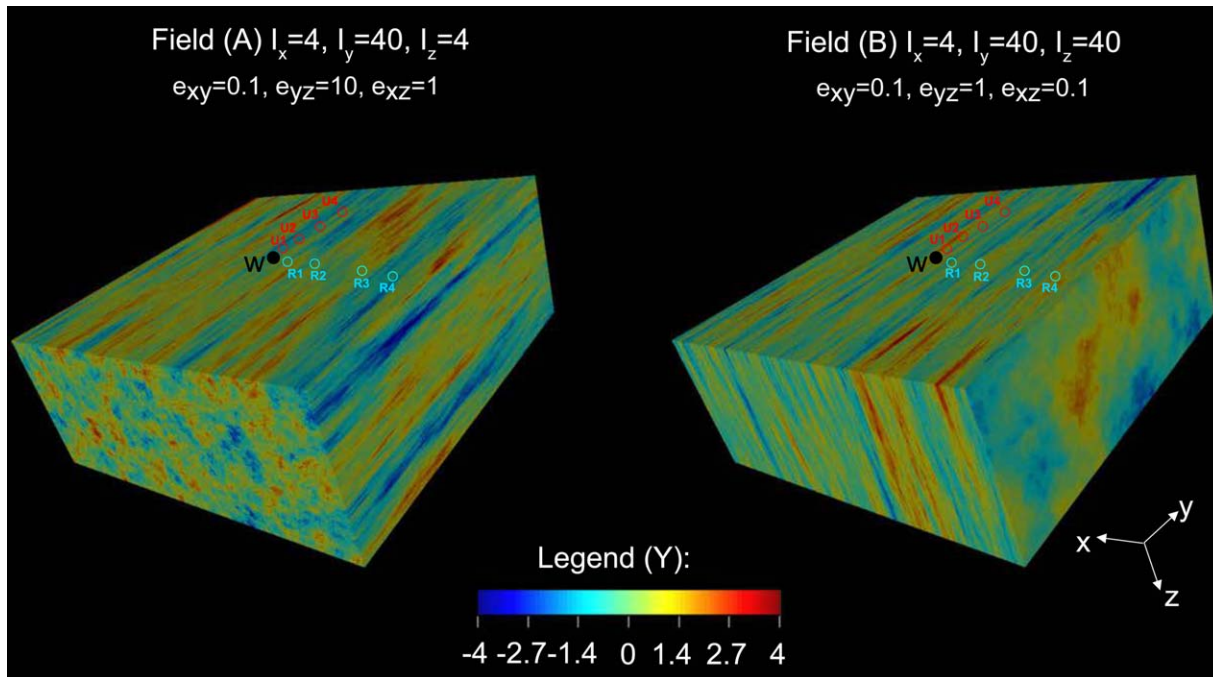
Figure 2. Example of simulations of different architecture of random hydraulic conductivity fields (a) and (b) reproducing the corresponding geological setups in Figure 1. I indicates integral scales and e anisotropy ratios of the integral scales. W marks the location of the fully penetrating pumping well, and R_i and U_i are the different injection locations ($i = 1, \ldots, 4$).

1. Fields (A) with enhanced correlation along a horizontal direction y ($I_y = 40$, $I_x = 4$, and $I_z = 4$, corresponding to $\epsilon_{xy} = 0.1$, $\epsilon_{xz} = 1$, and $\epsilon_{yz} = 10$).

2. Fields (B) with large correlation along two directions, those marked by the plane yz ($I_y = 40$, $I_x = 4$, and $I_z = 40$, corresponding to $\epsilon_{xy} = 0.1$, $\epsilon_{xz} = 0.1$, and $\epsilon_{yz} = 1$).

Examples of these fields are illustrated in Figure 2, where it can be seen on the top-left that field (A) corresponds to a geologic setting similar to the one reported in Figure 1(top left), while field (B) more closely resembles the outcrop in Figure 1(top right).

Transport is simulated using a random-walk approach (using code RW3D) [*Fernàndez-Garcia et al.*, 2005; *Salamon et al.*, 2007]. At time zero particles are introduced into the system as a vertical line using a flux-weighted scheme. Figure 2 highlights the eight specific injection locations that are chosen for analysis of the BTCs:

Injection points $U1$, $U2$, $U3$, $U4$ are oriented collinear with the y axis, at the same x coordinate of the well and at distances, respectively, of $R = 5, 12.5, 25, 75$ units from the well.

Injection points $R1$, $R2$, $R3$, $R4$ are oriented collinear with the x axis, at the same y coordinate of the well and at distances, respectively, of $R = 5, 12.5, 25, 75$ units from the well.

Using particle tracking methods, depth-integrated time-dependent concentrations ($C(t)$) are measured at the extraction well (i.e., the BTCs); these are equivalent to particle density functions ($\hat{p}$) estimated from the arrival time distributions of particles at the well. This is achieved assuming that

$$\hat{p}(t) = \frac{QC(t)}{\int QC(t)\mathrm{d}t}. \tag{1}$$

To resolve the curves adequately without using a prohibitively large number of particles we used a kernel density estimator (*KDE*) approach described in *Pedretti and Fernàndez-Garcia* [2013]. This technique is based on optimized Gaussian kernel functions that reconstruct BTCs from a limited particle data set. *KDE* is especially effective in capturing features of heavy-tailed BTCs in an efficient manner. After some preliminary

runs it was found that adequate, converged results were obtained with $N_P = 10^4$ particles and an adaptive weighting factor $\alpha = 0.5$ (see *Pedretti and Fernàndez-Garcia* [2013] for details on the selection of α).

2.2. Definition and Estimation of the Directional Capacity Coefficient

A common approach to upscale anomalous transport in heterogeneous aquifers is by means of MRMT solutions. The models assume the presence of different volumes within an individual cell where water either flows (mobile zones) or does not flow (immobile zones). There is a linear mass transfer of solutes between these zones and each zone is characterized by a particular mass-transfer coefficient. The flexibility of this model arises from the distribution of the mass-transfer coefficients, which weight the relationship between immobile and mobile zones over the time (i.e., the temporal storage of solute in the immobile zones). Several distributions have been postulated to include multiple domains with continuous or discrete distributions of mass-transfer parameters [e.g., *Haggerty and Gorelick*, 1995; *Cameron and Klute*, 1997; *Carrera et al.*, 1998; *Haggerty et al.*, 2000]. A mathematical formulation for a multirate mass-transfer model under radial coordinates (r-MRMT) reads

$$\frac{\partial C_m}{\partial t} + \beta \Gamma(C_m, r, t) = v_m(r) \frac{\partial C_m}{\partial r} + \frac{a_r v_m(r)}{r} \frac{\partial}{\partial r} \left(\frac{1}{r} \frac{\partial C_m}{\partial r} \right) \tag{2}$$

where β is the capacity coefficient, which is given by $\beta = \phi_{im}/\phi_m$. C_m is the solute concentration in the mobile (flowing) zone, a_r is the (longitudinal) dispersivity, v_m is a representative (mean) mobile velocity, and $\Gamma(C_m, r, t)$ is a sink-source term which accounts for the mass-transfer from and to the immobile zones. From (2), β sets the amount of mass that can be stored in the immobile domain. It does not control the shape of the concentration curve at late-times; this is controlled by the memory function embedded in Γ [e.g., *Carrera et al.*, 1998]. In general, the time corresponding to the peak in a BTC is controlled by the value of ϕ_m ("mobile porosity"), while the mean arrival time is controlled by the total porosity ($\phi_m + \phi_{im}$), where ϕ_{im} is the "immobile porosity"). Note that alternative and equally valid formulations may embed β into the memory function; however, we prefer here to separate them for the sake of our analysis, as we mainly focus on the behavior of β.

Specifically, our focus here is on finding directional patterns of the apparent β from numerical simulations performed in fields (A) and fields (B) (Figure 2). One possible way of obtaining β would be to fit each of the experimental random BTCs by solving (2) directly to obtain a distribution of apparent best-fitting parameters. This approach is challenging and can result in inaccurate solutions as solving (2) is not always straightforward. Analytical solutions [e.g., *Haggerty and Reeves*, 2002] are usually restricted to a finite combination of parameters and can rely on numerical inversion of Laplace transformed solutions, which are prone to numerical instabilities. Other numerical techniques can be adopted instead [e.g., *Silva et al.*, 2009] but this can be computationally burdensome. Moreover for CFTTs, BTCs [e.g., *Pedretti et al.*, 2013] can display very different shapes from the typical BTCs that are implemented in existing codes [e.g., *Haggerty et al.*, 2000].

As an alternative to the full numerical solution, we propose an approximate, faster approach based on travel time moments that yields a unique value for β for each BTC. Because the first moment of solute travel time depends exclusively on β and not on the mass-transfer rate coefficients [*Valocchi*, 1985; *Goltz and Roberts*, 1987; *Harvey and Gorelick*, 1995; *Rubin et al.*, 1997], β can be directly found from BTCs using the ratio between the first moment and the mean mobile time (t_{MT}) as

$$\beta = \frac{\mu_t^1}{t_{MT}} - 1, \tag{3}$$

where μ_1^t is the first-moment of the travel time distribution defined as [*Aris*, 1956]

$$\mu_t^1 = \frac{\int t C(t) \mathrm{d}t}{\int C(t) \mathrm{d}t}. \tag{4}$$

The derivation of (3) is presented in Appendix A. Note that this solution is not practical for our purposes since it requires the estimation of t_{MT} from the BTCs. The latter is an additional apparent parameter that would be obtained after model fitting using (2) (similar to a fitting procedure to obtain β, as explained

above). It is convenient here to assume that $t_{MT} \approx t_m$ (i.e., the mean mobile time being similar to the peak time). This approximation results in

$$\beta \approx \frac{\mu_t^1}{t_m} - 1. \tag{5}$$

This approximate solution is more versatile as it involves t_m, which is more easily and uniquely identifiable from the estimated BTCs, and avoids a fitting procedure using (2). We tested and successfully verified the accuracy of this approximation against a classical fitting procedure. A small subset of illustrative examples is reported in Appendix B (supporting information).

3. Dimensionless Variables

To compare results let us define the following dimensionless variables. A dimensionless time, t_c, is calculated as

$$t_c = t/t_{adv}, \tag{6}$$

where

$$t_{adv} = \frac{\pi b \phi R^2}{Q} \tag{7}$$

represents the mean advection time for a solute to travel within an homogeneous cylindrical aquifer under convergent flow conditions using Dupuit's assumption [e.g., *Moench*, 1989]. Recall that that throughout the simulations, porosity is assigned a deterministic spatially constant value ($\phi = 0.1$).

Let us also introduce the normalized horizontal injection-extraction distance, defined as

$$r_\lambda = \frac{R}{I_r}, \tag{8}$$

where I_r is the integral scale collinear with the injection-extraction axis. For injection locations $R1$ to $R4$, this means $I_r = I_x$, while for injection locations $U1$ to $U4$, this means $I_r = I_y$. It is also important to compare the relative length of the injection line (which corresponds to the model thickness, b) with the vertical integral scale, I_z. A variable, L_z, is defined as

$$L_z = \frac{b}{I_z}. \tag{9}$$

The larger L_z, the more the solute is injected through a few preferential flow path, such as in fields (A); conversely, the smaller L_z, the more homogenized is the injection, such as in fields (B).

4. Statistical Features Controlling the Spatial Distribution of β

Our first goal was to understand if the apparent β depends on anisotropy when estimated from CFTTs. To achieve this, it is useful to first indicate whether useful phenomenological evidence can be obtained from statistical inference. Two hundred and fifty realizations of each field (A) and (B) were produced. In each one, particles were injected at different points drawn from a grid of points representing fully penetrating piezometers and tracked until they reached the well. The value of β was then estimated for each BTC using (5). From this a 2-D map was drawn indicating β at each injection point. To emphasize the widely contrasting values found and visually highlight the anisotropic structures, we present results as the logarithm (base 10) of the capacity coefficient (denoted log (β)).

The two resulting maps for the ensemble average of the log-transformed capacity coefficient, E (log (β)), from the 250 simulations of field (A) and field (B) are plotted in Figure 3. The structure of both maps is
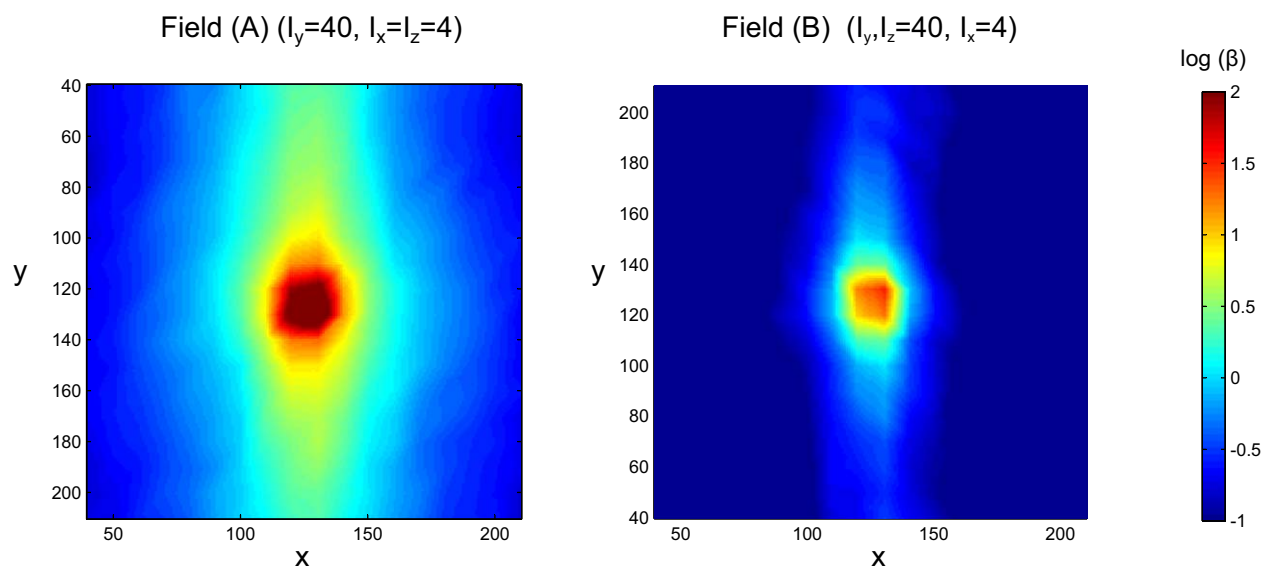
Figure 3. Map representing the logarithm (base 10) of the capacity coefficient (β), for fields (left) (A) and (right) (B); at each point the log (β) value is estimated from the BTC recorded from a tracer injected at that particular location.

clearly and qualitatively anisotropic. Only at injection locations close to the pumping well is no apparent anisotropic structure is visible. This is likely a combination of local isotropy of the blocks and the resolution of the numerical grid (discussed in more detail further on). From a quantitative perspective, although both log (β) maps are anisotropic, they show very distinct values, as emphasized by the use of a common color scale; note for instance that the log (β) map for field-type (A) displays fewer negative log (β) values, while such negative values are more common in field-type (B).

The quantitative difference between the maps presented in Figure 3 is associated with the different vertical integral scales L_z values, which are 10 times smaller in fields (A) as compared to those of fields (B). From a statistical perspective, this means that the ensemble statistics of fields (A) should display less variability than the ones of fields (B).

The distribution of the second moment of the experimental Monte Carlo distribution (not shown here) indicates that, while E (log (β)) is highly structured for both fields, this is not the case for the variance ($\sigma^2_{\log(\beta)}$). We observed no significant spatial organization for $\sigma^2_{\log(\beta)}$ values in either fields (A) and fields (B); the difference is found in the average values $\left(\overline{\sigma^2_{\log(\beta)}}\right)$ which was found to be smaller for fields (A) $\left(\overline{\sigma^2_{\log(\beta)}}=0.80\right)$ with respect to those for fields (B) $\left(\overline{\sigma^2_{\log(\beta)}}=1.12\right)$. Again, while the number of realizations (250) used to obtain these numbers might be considered small, we want to stress that the objective was to find whether the maps of β displayed a spatial structure at all, rather than finding the actual values of β at given locations.

From these results, it should be clear that from a statistical perspective, there is a clear dependence of the spatial anisotropic organization of log (β) on the structure of ln K. However, this result alone does not really explain what physical processes controls β for a given tracer test performed at a given location (x, y). A deeper understanding of this would be fundamental to understanding what soil parameters actually control the size of the mass-transfer capacity coefficient, which would give additional insights to understand how one might begin to build predictive versions of an MRMT model. This is explored in the following sections.

5. Exploring the Role of Connectivity in Controlling β

From the previous section, we know that apparent β values derived from individual tracer tests depend on L_z, but also on r_λ, because the structure of log (β) depends on whether the injection-extraction direction is collinear or orthogonal to the main planar anisotropic axis. When r_λ is small and/or L_z is large, transport can

be highly nonergodic, as the solutes sample only a relatively small portion of the heterogeneity between the injection and the extraction well. From a qualitative perspective, this gives rise to connected structures, which may influence the distribution of particle travel times.

Some of these concepts have been recently discussed by *Pedretti et al.* [2013], who analyzed the apparent joint effects of stratification and connectivity due to lack of ergodicity in these systems. In addition, *Pedretti et al.* [2013] showed that the concentration peaks obtained after analyzing particle travel times transported over different layers in 3-D formations are very representative of the total connectivity of the system from the injection point to the extraction well, as related by the system stratification. Similar concepts are used here to explain the quantitative link that exists between directional connectivity and the apparent directional capacity coefficient.

This part of the study is based on the concept of "*point-to-point connectivity*" [e.g., *Knudby and Carrera*, 2006; *Trinchero et al.*, 2008]. For the specific case of convergent radial transport, this method postulates that a *dynamic* connectivity indicator [*Renard and Allard*, 2013] can be obtained from the relative temporal scaling of the BTCs peak time (t_m) in a heterogeneous medium compared to an equivalent homogeneous medium. Recall the definition of dimensionless time used in this analysis (6); in an homogeneous field all BTCs plotted on a double-log plot would be symmetric around the concentration peak, which would occur at $t_c = 1$. Similarly, connectivity can be quantitatively measured as the relative position of t_m with respect to $t_c = 1$: the shorter the peak time ($t_m/t_c < 1$), the more hydraulically connected are the injection-extraction wells; and vice versa, the larger the peak time ($t_m/t_c > 1$), the less connected are these two locations. We direct the interest reader to the cited works for a more exhaustive description of these concepts.

5.1. Qualitative Analysis

First, let us focus on qualitative aspects of the BTCs (from which β is obtained) associated with two orthogonal injection points $R4$ and $U4$. These are located at the same distance from the well ($R = 75$ cells), but have different r_λ values. For these cases, 1000 realizations are simulated, and all the BTCs for these two injection locations are depicted in Figure 4. Plots are presented one a double-log axis to emphasize any anomalous late-time behavior.

On Figure 4 (top left), we plot the BTCs associated with injection point R4 ($r_\lambda = r/l_x = 18.75$) in fields of type (A) ($L_z = 25$). As one might expect, we observe that most curves are located around $t_c = 1$ (marked by the vertical dashed line), and only a few show significantly different peak times. This also means, consistent with the above definition of connectivity, that from this graph only a few simulations offer a noticeable deviation from the homogeneous case, and thus there is a limited effect of connected features. For illustrative purposes, we highlight with different colors three individual BTCs, representing, respectively, highly connected, mildly connected, and less connected simulations. The red line highlights the BTCs from a realization showing one of the shortest peak times ($t_c \ll 1$) found in the ensemble of BTCs, indicating the highest degree of connectivity among all cases. In this well-connected case, the BTC displays a fast early arrival time followed by a prolonged late-time tailing behavior. Tailing in this case is defined as the persistent slope observed on these plots. Tailings seems to scale as straight line in double-log plots, thus similar to power-law distributions; however, since most of the BTCs span only a few logarithmic time cycles, caution should be taken when inferring a power-law distribution in this narrow time interval [e.g., *Clauset et al.*, 2007].

A similar behavior can be seen on the BTC represented by the blue line. Here the peak time is closer to $t_c = 1$ than for the red curve, and the anomalous tailing is less defined than in the previous case (indeed for this case, no apparent power-law behavior can be easily identified). In the other highlighted realization, the peak of the black BTC occurs at $t_c > 1$ and the shape of the curves appears more symmetric (like an homogeneous case). The behavior of the latter curve is also representative of the majority of BTCs within the ensemble, thus indicating that only a few cases display anomalous behavior, defined by the nonsymmetric nature of the BTCs.

A different behavior is observed when the injection location switches to U4 ($r_\lambda = r/l_y = 1.88$) on the same fields (A). These plots are shown at the top-right of Figure 4. The solute travels <2 integral scales to the extraction well. The main difference with respect to the curves when the tracer is injected at R4 is that most of the BTCs display peak times shorter than $t_c = 1$ (indicating higher connectivity), and most of them also
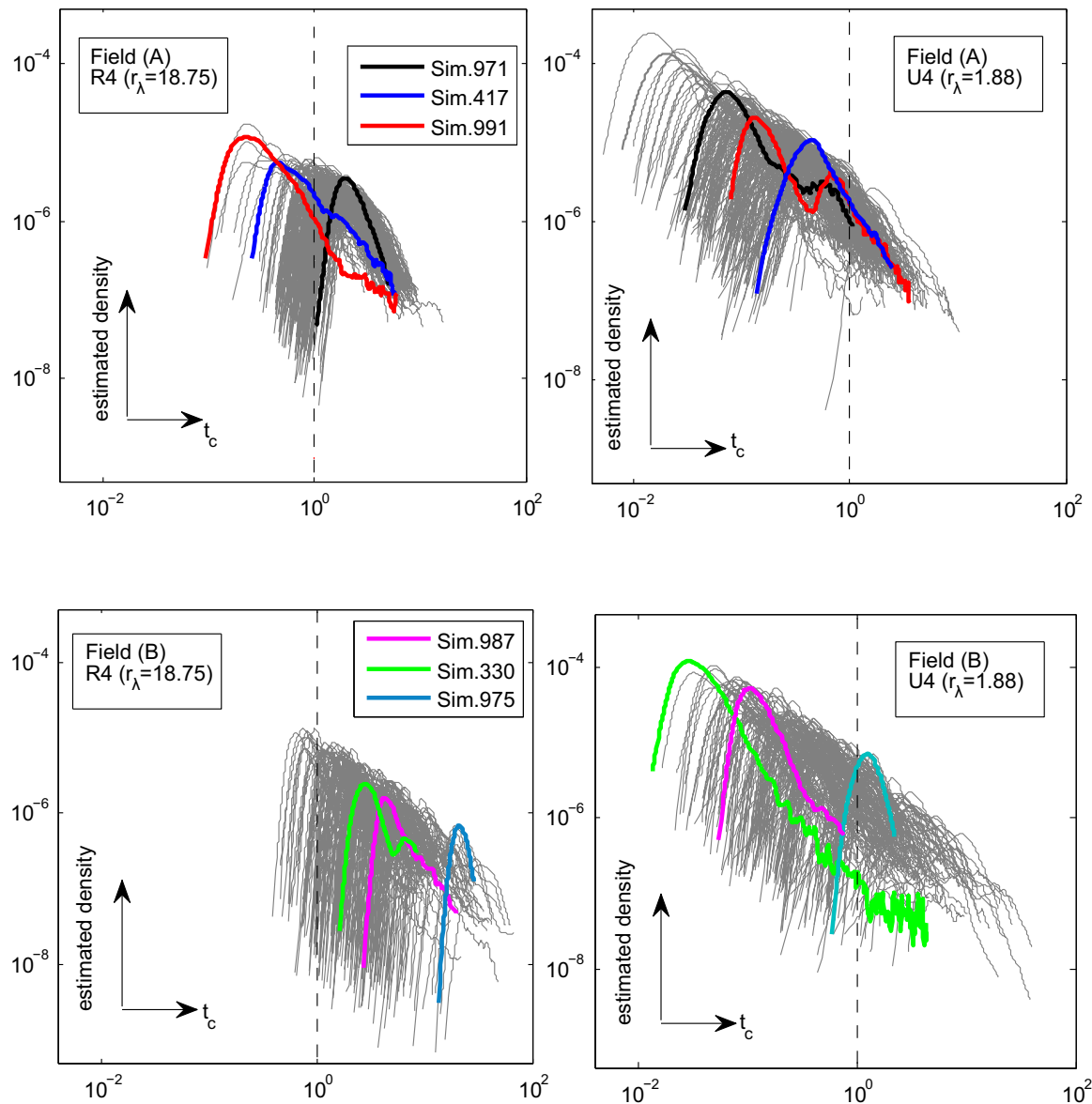
Figure 4. Ensemble of 1000 estimated density functions obtained after injecting particles at two different locations, (right) R4 and (left) U4 in fields (top) (A) and fields (bottom) (B). All plots show the same axis lengths to emphasize the different shape depending on the field and the injection locations. Time t_c is dimensionless (see text). Colored curves correspond to individual selected realizations and are only highlighted to show different shapes.

display heavy tailing. Looking at the same four fields discussed for the previous location, it can be seen the peak times of all these BTCs are lower than $t_c = 1$. Even for this location it can be seen than the qualitative relationship between peak time (connectivity) and development of asymmetric tailing can be observed, meaning that, also for this case, as a general rule simulations where the peak time is smaller are also those displaying stronger tails.

On the bottom of Figure 4, we show the BTCs obtained from injection locations R4 and U4, respectively, for field (B) ($L_z = 2.5$). Here the effect of the vertical homogenization of the injection can be seen, observing that at R4 BTCs look more symmetric in field (B) than their counterparts in field (A). However, BTCs from point U4 still display the strong effects of connectivity. We highlight three specific and representative cases for fields (B). Violet and light-blue curves represent fields where BTCs are quasisymmetric for both R4 and U4 injection locations. It can be seen that at U4 the violet BTCs display, at very late-time, anomalous tailing for a very limited time extent. On the other hand, the green line at U4 displays strong anomalous behavior

with a heavy-tailed distribution; once again, this is the case with the highest degree of connectivity from this ensemble.

5.2. Quantitative Analysis

We qualitatively observed from the previous section that larger nonsymmetric distributions (larger β) are found when connectivity was also larger (lower t_m). To seek a more quantitative description of the relationship between β and connectivity, let us first observe the statistics of the distribution of the three main transport variables considered in this analysis (β, t_m, and μ_t^1) for locations R1 to R4 and for locations U1 to U4, for both fields (A) and (B). The application of a chi-squared test suggests that all these distributions are lognormal (α-level of significance equal to 5%), so that for each parameter we report the statistics of the log-transformed counterpart.

The complete results of these statistics are reported in Tables S1 and S2 (supporting information). We observe that these data have large uncertainty around the mean values (reflected by the large *CV* value). This is true particularly for fields (B) (e.g., at point U3), confirming that the large integral scales applied both in the horizontal and the vertical directions relative to injection distance from the well and domain thickness result in lack of ergodicity in the transport solutions, making the ensemble a somewhat meaningless measure with poor applicability for predictive purposes. On the other hand, for fields (A), such variability is much lower, and the ensemble means are more representative of the BTCs recorded in each realization than in the previous case.

Comparing how these variables are correlated by pairs, we can observe that a robust relationship appears to exist between β and the connectivity indicator t_m for fields (A) and position $R4$ (Figure 5−1). The best-fit model using a linear least-square regression method for this correlation turned out to be an exponential model with a Pearson's coefficient of $R^2 = 0.61$ and a low root mean square error (RMSE). The correlation highlights that the higher the connectivity, the larger β; and vice versa. That means that a weak (apparent) separation of transport in mobile and immobile zones occur for less connected points; as connectivity increases (shorter t_m), β increases, indicating a higher degree of (apparent) separation in mobile/immobile subdomains.

This inverse dependence between β and connectivity is still visible for injections associated with point $U4$ in fields (A) (Figure 5−2), but with a much higher degree of uncertainty (larger RMSE and much smaller R^2 than the $R4$ case). In this case, all values are found between $\beta = 1$ and $\beta = 10$. Another important aspect shown in Figures 5−3 and 5−4 is that β appears very poorly correlated with μ_t^1, even though Figures 5−5 and 5−6 indicate that there exists a strong correlation between the t_m and μ_t^1. The fact that t_m and β are better correlated than μ_t^1 and β is linked to the propagation of errors of the correlation between t_m and μ_t^1. This issue is consistent with our analysis, since t_m is a better estimator of connectivity than μ_t^1, and connectivity has greater influence on β than the position of the center of mass. This is similar to the observations drawn the individual realization analysis, which will be provided in the next section.

For fields (B) (Figure 6), the correlation between variables for both injection locations for $R4$ and $U4$ is generally worse. In this field, no significant correlation is found between β and connectivity (Figures 6−1 and 6−2), nor between β and μ_t^1 (Figures 6−3 and 6−4). Similar to what was observed for field (A), on the other hand, there is a solid relationship between t_m and μ_t^1 (Figures 6−5 and 6−6). This is explained again by the fact that the realizations from fields (B) display much less vertical variability of K. Particle injection and transport is much more homogenized, on average, for fields (B) than in fields (A). This also indicates that the flux-weighted injection that happens preferentially in small channels (low L_z) rather than in more homogenized formations (high L_z) is a fundamental aspect controlling the dependence of β on the connectivity.

This general behavior is in line with other previous studies on anisotropic formations under uniform flow, which pinpoint the relationship between tailing and statistical anisotropy of the system [e.g., *Guswa and Freyberg*, 2002]. Our results extend the analysis by *Pedretti et al*. [2013] and *Pedretti and Fiori* [2013] which highlighted the importance of stratification on tailing under convergent radial flow. In *Pedretti et al*. [2013], it was observed that the formation of tailing on BTCs is controlled primarily by the dimensionless injection distance r_λ. When $r_\lambda \approx 1$, such as in the case of injections $U4$, particles travel only a few integral scales and are thus subjected to plume stratification. As the difference in connectivity among layers becomes more important, the solute tends to be more stratified, giving rise to a larger separation of the peak time from
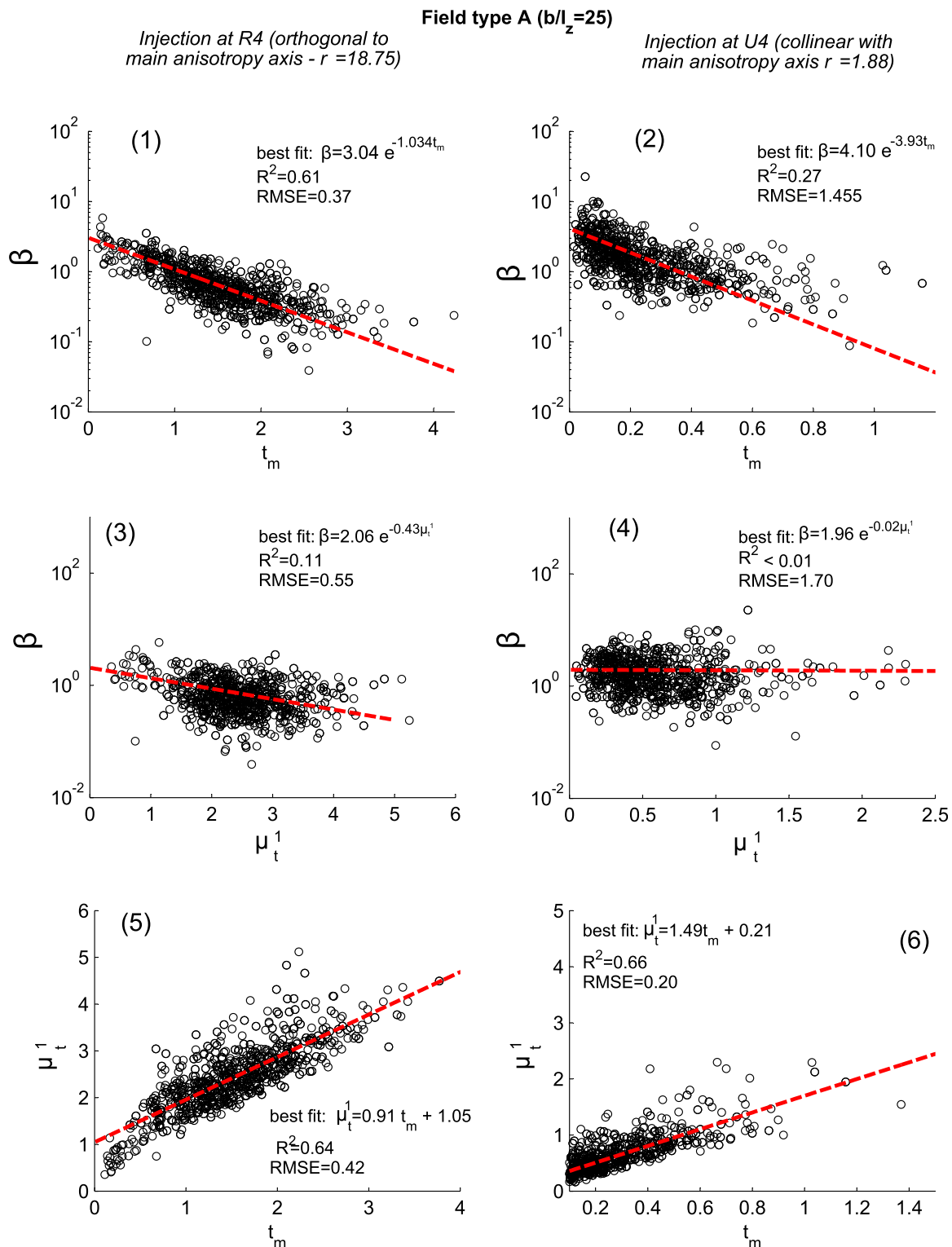
Figure 5. Correlation between β, t_m, and μ_t^1 at locations R4 and U4 (all simulations for fields (A) are plotted). The red line represents the best-fitting curve for each case. RMSE = root mean square error, R^2 = Pearson coefficient.

the center of mass of the plume (i.e., β). As the injection distance approaches 0, the injected plume becomes perfectly stratified and β is largest. The anisotropic distribution of β is therefore a consequence of the ability of the injected solute to be stratified around the well.
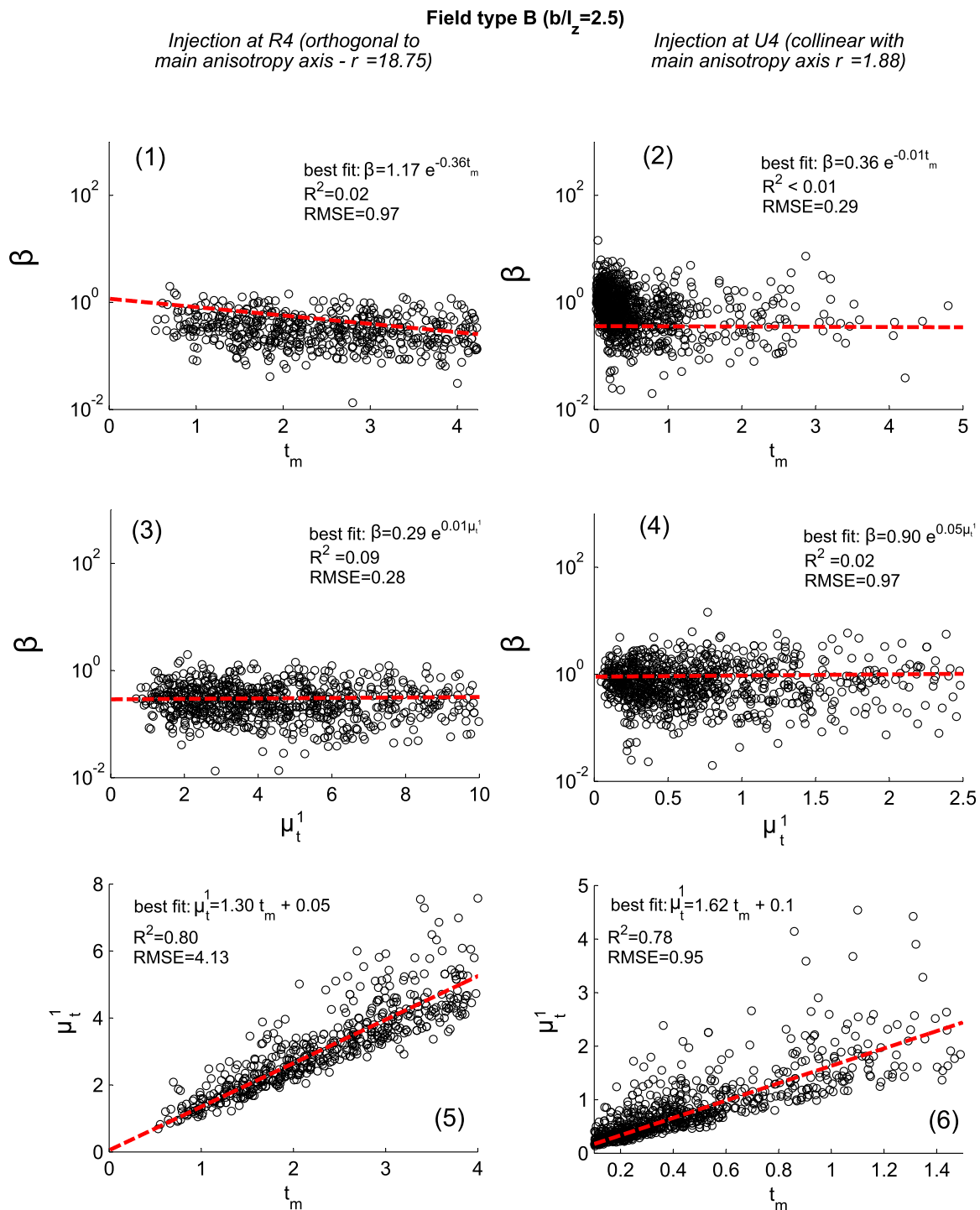
Field type B (b/l$_z$=2.5)

Injection at R4 (orthogonal to
main anisotropy axis - r =18.75)

Injection at U4 (collinear with
main anisotropy axis r =1.88)

Figure 6. Correlation between β, t_m, and μ_t^1 at locations R4 and U4 (all simulations for fields (B) are plotted). The red line represents the best-fitting curve for each case. RMSE = root mean square error, R^2 = Pearson coefficient.

Consequently, we observed here that the physical link between β and K is related to the statistical heterogeneity scales, which control the tradeoff between vertical mixing and transport stratification. Vertical mixing tends to homogenize the transport and thus renders BTCs more symmetric; this occurs when the dimensionless injection distance $r_\lambda \gg 1$. On the other hand, the variable connectivity of the layer composing the formation (intimately related to stratification) tends to maintain a separation of the contribution to each single layer of the depth-integrated BTCs, as explained in *Pedretti et al.* [2013]; this occurs when $r_\lambda \approx 1$. In
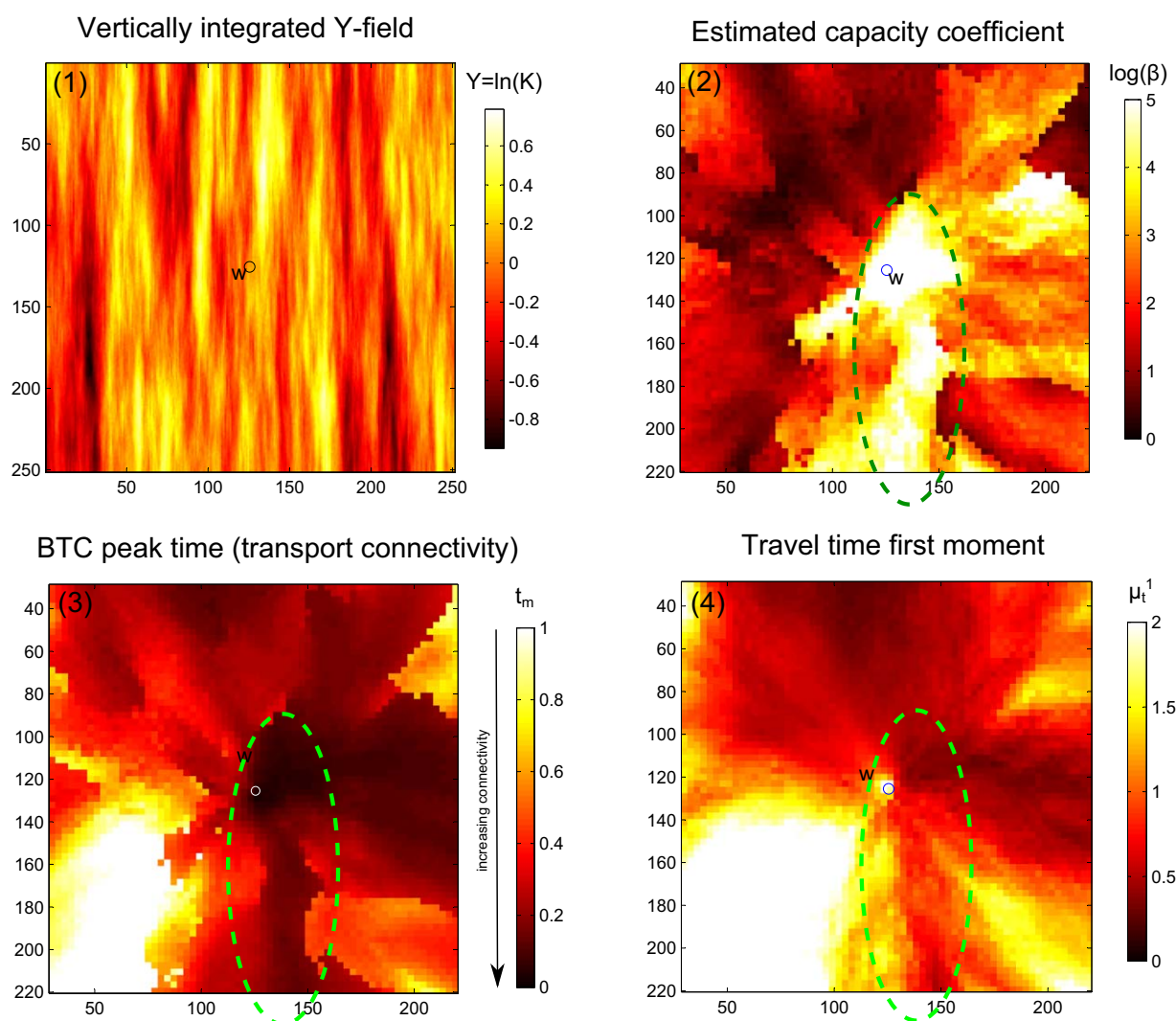
Figure 7. Visual relationship between anisotropic structure, connectivity, and mass-transfer capacity coefficient for one individual realization of fields (A). Maps reproduce (1) the vertically integrated log-transformed hydraulic conductivity; (2) the capacity coefficient β (in log_{10}); (3) the BTC peak time t_m (or the map of connectivity—inversely proportional to t_m), and (4) the advection time μ_t^1. "W" indicates the position of the well. The ellipse highlights the most connected channel in map (3) with correspondingly large log (β) found in map (2) (see discussion in the text).

addition, the shorter the injection distance compared to the vertical domain size (fields (A)), the more significant this stratification effect is; therefore, the vertical dimensionless injection length also plays a fundamental role in determining the ability of the system to separate apparent mobile and immobile transports under convergent radial flow.

6. What Happens in an Individual Random Realization?

From our observations, so far we conclude that there exists a correlation between connectivity and β in a statistical sense. From a qualitative perspective, our conclusion matches those of *Zinn and Harvey* [2003] and *Willmann et al.* [2008], among others, but here we have also quantified this dependence. This is a critical issue because it provides a physical explanation for a mass-transfer parameter, β, derived in advection-dominated problems. This is promising in the path toward improving the predictive capacity of models in these types of transport regimes.

To test how generally true our findings are and to what extent they hold, we now analyze what happens in an individual realization. We chose one random realization selected from the ensemble of field (A). We ran a CFTT with an injection at each (x, y) grid location and explored the correlation of β, t_m, and μ_t^1. For the
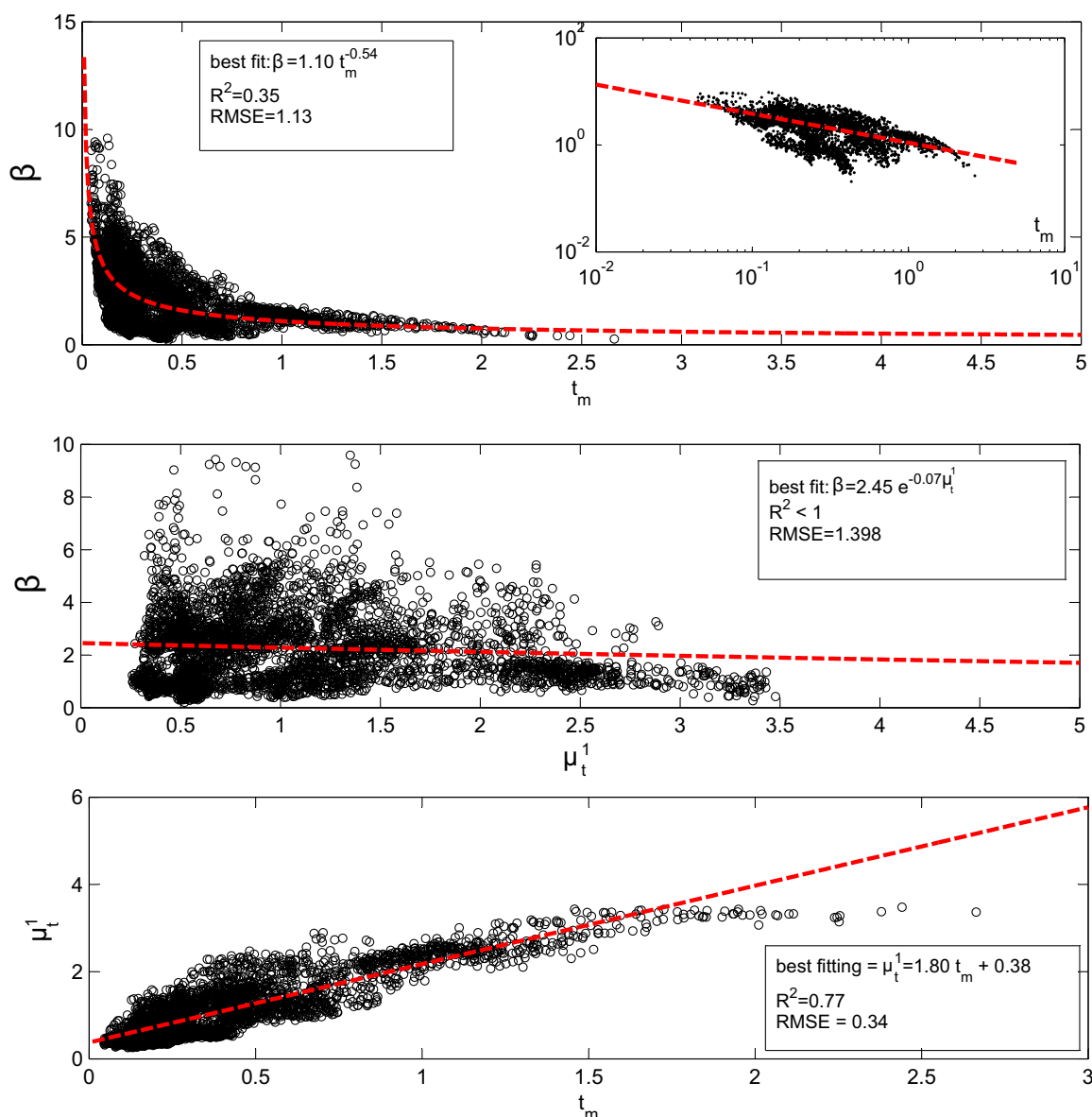
Figure 8. Correlation between β, t_m, and μ_t^1 for the individual realization analysis (all injection points are plotted). The red line represents the best-fitting curve for each case. RMSE = root mean square error, R^2 = Pearson coefficient.

single realization case, we compared the values obtained for all (x, y) pairs, including those points close to the well.

The resulting β map for this field is shown in Figure 7-2. For comparison purposes, we also plotted the vertically averaged ln K for this chosen field (Figure 7-1), as well as the maps for μ_t^1 (Figure 7-4) and t_m (Figure 7-3). The latter represents also the "point-to-point connectivity" map, as point-to-point connectivity is directly related to the inverse of the BTC peak time, as explained in the previous sections. Visually, all three plots display certain structural similarities, although μ_t^1 appears much smoother than the other two; this is due to the fact that the average time taken by the plume to migrate from the injection to the extraction point is not only influenced by the irregular random shape of preferential channels (fast flow zones) but is dispersed into all the less mobile zones between the two points in a more continuous way.

Larger β and t_m values in the maps show a channeled structure along the y axis (brighter and darker colors, respectively, in the relative maps, also highlighted by the green ellipse drawn on the maps), which is also

the main preferential statistical correlation of Y used to build this field. Conversely, lower β values are found in the presence of larger BTCs peak times, such as in the lower-left regions of these maps.

To quantify our purely visual inferences of correlations in the previous paragraph, in Figure 8, we plot bivariate plots of β, t_m, and μ_t^1 and present best-fit models of this data (as for the ensemble analysis). It was found that a power-law function is the best-fit model when t_m is plotted against the two other variables. However, the Pearson coefficient R^2 is low, indicating large dispersion of data around the power-law trend. Also, no significant correlation between β and μ_t^1 was found, indicating that the distribution of advection time does not control the distribution of the capacity coefficient as significantly as connectivity does. This is despite the fact that advection and mobile times have a much stronger correlation, as shown in the bottom plot of Figure 8.

As such, connectivity is the primary responsible factor for the distribution β, also in this individual realization. This suggests that it is the physical parameter that most strongly controls the apparent mass-transfer parameter.

Single-realization correlations are smaller than those of the ensemble. Measurements corresponding to all locations in the map are plotted together, while in the ensemble analysis we focused on several random outcomes from a few injection locations; the development of tailing due to heterogeneity is largely controlled by the relative injection distance for CFTTs, as shown by *Pedretti et al.* [2013].

7. Conclusions

Upscaling of anomalous transport in heterogeneous formations under radially convergent flow is a complex issue; it is important for making practical and effective decisions for risk assessment and remediation of polluted heterogeneous aquifers [*Bolster et al.*, 2009; *de Barros et al.*, 2011]. We conducted a numerical study to check the existence of phenomenological links between the capacity coefficient β (which is an important parameter used in common upscaling approaches), and the directional-dependent statistical correlation of the natural log-transformed hydraulic conductivity, Y. This link is only apparent (hence the name of "apparent capacity coefficient") since formally speaking β is mathematically based on diffusive-like mass transfer processes giving rise to anomalous transport, while the latter occurs in our analysis under advection-dominated conditions.

We developed a quick and efficient method to estimate β, demonstrated in Appendix B, which is expressed as the ratio between the first moment of the arrival time distribution and the concentration peak time from each breakthrough curve. The latter provides an indication of "point-to-point connectivity," i.e., how fast/slow the response time is between the injection and the extraction locations during a convergent-flow tracer tests. We measured this parameter after reconstructing BTC peak times from particle travel time distributions after being injected at different locations in a convergent flow radial setup.

Our analysis spanned both individual and a representative ensemble of realizations from two different types of anisotropic fields. Among them, we analyzed fields showing preferential correlation along one planar axis, thus resembling a stream-channeled system, and fields showing preferential correlation along the planar axis and the vertical direction, thus resembling vertically tilted fractures.

Our simulations help to illustrate that β effectively displays an apparent directional behavior in anisotropic formations, for both types of fields. The directionality of β is remarkable, since β is usually adopted as an isotropic parameter in nonlocal formulations used to fit BTCs from tracer tests in heterogeneous media. The key aspect is that β behaves in a qualitatively similar manner to the anisotropic distribution of K, thus proving that a link between physical (K) and mathematical (β) can be built in the limit of CFTTs in anisotropic formations.

Our setup is far from ergodic transport and therefore unlikely to provide universally exportable quantitative conclusions. Nonetheless, two main parameters seem to play a major role in controlling the behavior of β:

(1) the dimensionless parameter r_λ, which expresses the ratio between travel distance (radius between the injection and the extraction locations) relative to the underlying correlation distances. This result is in agreement with the analysis by *Pedretti et al.* [2013], who found that r_λ is a characteristic value indicating the

apparent effect of stratification in controlling anomalous tailing in BTCs during convergent flow tracer tests. The more stratified the injection, the larger β; as a consequence, β is maximum as $r_\lambda \rightarrow 0$ (perfectly stratified transport), while β tends to a minimum value as $r_\lambda \rightarrow \infty$ (due to effects of vertical mixing and plume homogenization);

(2) the dimensionless parameter l_z, which sets the relative "homogenization" during the injection of the solute in the aquifer. It was found that the ensemble mean values for β for fields (A) are substantially different (generally lower) from those for fields (B).

A more detailed analysis showed that a strong relationship may exist between β and BTC peak times. This relationship is stronger for fields (A) than fields (B), which is consistent with the fact that when the injected solutes are less homogenized (fields A), solutes tends to be more stratified, giving rise to more transport variability between layers making up the aquifer. This is consistent with the analysis of *Pedretti et al.* [2013].

We can conclude from our analysis that these results give new insights into understanding how to relate upscaled parameters to physical soil parameters, which is a critical step to understanding how to adequately use these effective solutions for predictive purposes. In this type of setting, connectivity and stratification, which are intimately related, seem to determine how likely the system tends to behave as an apparent single-porosity or multiporosity domain. From a practical perspective, the directional behavior of β in anisotropic settings provides empirical evidence of physical constraints to one of the parameters used in multirate mass-transfer models, which to date have not been proven to be predictive under advection-dominated transport conditions.

Appendix A: Derivation of (5)

Benson and Meerschaert [2009] show that the continuum MRMT equation is equivalent to a two-state Markov chain model wherein a particle transfers between mobile and immobile states. They show that a particle has exponentially distributed mobile times M (with mean $1/\beta\lambda$), and random times in the immobile phase W with mean waiting time (if it is well defined) of $1/\lambda$. This defines β in this model as the ratio of mean times in the immobile and mobile zones $\left(\frac{1}{\lambda} / \frac{1}{\beta\lambda} = \beta\right)$. We may define the first arrivals as those particles that spend little or no time in the immobile phase with arrival time $\sum M_i$ and those particles that spend ample time in the immobile zone on their journey as having mean arrival time $\sum M_i + W_i$. Taking expectations and the ratio, and eliminating the sum (which is an identical number for each):

$$\frac{\sum E[M_i] + E[W_i]}{\sum E[M_i]} = \frac{1/\beta\lambda + 1/\lambda}{1/\beta\lambda} = 1 + \beta = \frac{\mu_t^1}{t_{MT}} \tag{A1}$$

On the far right-hand side, we recognize that the mean arrival time is the sum of the mean mobile and mean immobile times. Note that β is independent of any mass-transfer rate distribution or memory functions.

References

Aris, R. (1956), On the dispersion of a solute by diffusion, convection and exchange between phases, *Proc. R. Soc. London, Ser. A, 252*(1271), 538–550, doi:10.1098/rspa.1959.0171.

Becker, M., and A. M. Shapiro (2000), Tracer transport in fractured crystalline rock: Evidence of nondiffusive breakthrough tailing, *Water Resour. Res., 36*, 1677–1686.

Benson, D. A., and M. M. Meerschaert (2009), A simple and efficient random walk solution of multi-rate mobile/immobile mass transport equations, *Adv. Water Resour., 32*, 532–539, doi:10.1016/j.advwatres.2009.01.002.

Bolster, D., M. Barahona-Palomo, M. Dentz, D. Fernàndez-Garcia, X. Sanchez-Vila, P. Trinchero, C. Valhondo, and D. M. Tartakovsky (2009), Probabilistic risk assessment applied to contamination scenarios in porous media, *Water Resour. Res., 45*, W06413, doi:10.1029/2008WR007551.

Cameron, D. R., and A. Klute (1997), Convective-dispersive solute transport with a combined equilibrium and kinetic adsorption model, *Water Resour. Res., 13*, 183–188, doi:10.1029/WR013i001p00183.

Carrera, J., X. Sanchez-Vila, I. Benet, A. Medina, G. Galarza, and J. Guimerà (1998), On matrix diffusion: Formulations, solution methods and qualitative effects., *Hydrogeol. J., 6*, 178–190, doi:10.1007/s100400050143.

Clauset, A., C. R. Shalizi, and M. E. Newman (2007), Power-law distribution in empirical data, *SIAM Rev., 51*, 661–703, doi:10.1137/070710111.

Dagan, G. (1989), *Flow and Transport in Porous Formations*, Springer, Berlin.

de Barros, F. P., D. Bolster, X. Sanchez-Vila, and W. Nowak (2011), A divide and conquer approach to cope with uncertainty, human health risk, and decision making in contaminant hydrology, *Water Resour. Res.*, *47*, W05508, doi:10.1029/2010WR009954.

Donado, L. D., X. Sanchez-Vila, M. Dentz, J. Carrera, and D. Bolster (2009), Multicomponent reactive transport in multicontinuum media, *Water Resour. Res.*, *45*, W11402, doi:10.1029/2008WR006823.

Fernàndez-Garcia, D., X. Sanchez-Vila, and T. H. Illangasekare (2002), Convergent-flow tracer tests in heterogeneous media: Combined experimental-numerical analysis for determination of equivalent transport parameters, *J. Contam. Hydrol.*, *57*(1–2), 129–145, doi:10.1016/S0169-7722(01)00214-5.

Fernàndez-Garcia, D., T. H. Illangasekare, and H. Rajaram (2004), Conservative and sorptive forced-gradient and uniform flow tracer tests in a three-dimensional laboratory test aquifer, *Water Resour. Res.*, *40*, W10103, doi:10.1029/2004WR003112.

Fernández-Garcia, D., H. Rajaram, and T. H. Illangasekare (2005), Assessment of the predictive capabilities of stochastic theories in a three-dimensional laboratory test aquifer: Effective hydraulic conductivity and temporal moments of breakthrough curves, *Water Resour. Res.*, *41*, W04002, doi:10.1029/2004WR003523.

Fiori, A., I. Jankovic, and G. Dagan (2006), Modeling flow and transport in highly heterogeneous three-dimensional aquifers: Ergodicity, Gaussianity, and anomalous behavior-2. Approximate semianalytical solution, *Water Resour. Res.*, *42*, W06D13, doi:10.1029/2005WR004752.

Flach, G. (2012), Relationship between dual-domain parameters and practical characterization data, *Ground Water*, *50*(2), 216–229.

Gelhar, L. W. (1993), *Stochastic Subsurface Hydrology*, Prentice-Hall, Englewood Cliffs, N. J.

Gelhar, L. W., A. L. Gutjahr, and R. L. Naff (1979), Stochastic analysis of macrodispersion in a stratified aquifer, *Water Resour. Res.*, *15*, 1387–1397.

Goltz, M. N., and P. V. Roberts (1987), Using the method of moments to analyze three-dimensional diffusion-limited solute transport from temporal and spatial perspectives, *Water Resour. Res.*, *23*, 1575–1585, doi:10.1029/WR023i008p01575.

Gouze, P., Y. Melean, T. Le Borgne, M. Dentz, and J. Carrera (2008), Non-Fickian dispersion in porous media explained by heterogeneous microscale matrix diffusion, *Water Resour. Res.*, *44*, W11416, doi:10.1029/2007WR006690.

Guswa, A. J., and D. L. Freyberg (2002), On using the equivalent conductivity to characterize solute spreading in environments with low-permeability lenses, *Water Resour. Res.*, *38*(8), 7-1–7–14, doi:10.1029/2001WR000528.

Haggerty, R., and S. Gorelick (1995), Multiple-rate mass transfer for modeling diffusion and surface reactions in media with pore-scale heterogeneity, *Water Resour. Res.*, *31*, 2383–2400, doi:10.1029/95WR10583.

Haggerty, R., and P. C. Reeves (2002), STAMMT-L: Solute Transport and Multirate Mass Transfer, version 1. 0, user's manual, Rep. ERMS520308, Sandia Natl. Lab., Albuquerque, N. M.

Haggerty, R., S. A. McKenna, and L. C. Meigs (2000), On the late-time behavior of tracer test breakthrough curves, *Water Resour. Res.*, *36*, 3467–3479, doi:10.1029/2000WR900214.

Harvey, C. F., and S. Gorelick (1995), Temporal moment-generating equations: Modeling transport and mass transfer in heterogeneous aquifers, *Water Resour. Res.*, *31*, 1895–1911, doi:10.1029/95WR01231.

Knudby, C., and J. Carrera (2006), On the relationship between indicators of geostatistical, flow and transport connectivity, *Adv. Water Resour.*, *28*(4), 405–421, doi:10.1016/j.advwatres.2004.09.001.

Koltermann, C. E., and S. Gorelick (1996), Heterogeneity in sedimentary deposits: A review of structure-imitating, process-imitating, and descriptive approaches, *Water Resour. Res.*, *32*, 2617–2658.

Le Borgne, T., M. Dentz, and J. Carrera (2008), Lagrangian statistical model for transport in highly heterogeneous velocity fields, *Phys. Rev. Lett.*, *101*, 090601.

Matheron, G. (1967), *Elements Pour Une Theorie des Milieux Poreux*, Masson et Cie, France.

Moench, A. (1989), Convergent radial dispersion: A Laplace transform solution for aquifer tracer testing, *Water Resour. Res.*, *25*, 439–447, doi:10.1029/WR025i003p00439.

Neuman, S. P., and D. M. Tartakovsky (2009), Perspective on theories of non-Fickian transport in heterogeneous media, *Adv. Water Resour.*, *32*, 670–680.

Nkedi-Kizza, P., J. W. Biggar, H. M. Selim, M. T. Van Genuchten, P. J. Wierenga, J. M. Davidson, and D. R. Nielsen (1984), On the equivalence of two conceptual models for describing ion exchange during transport through an aggregated oxisol, *Water Resour. Res.*, *20*, 1123–1130, doi:10.1029/WR020i008p01123.

Parker, J. C., and M. T. Van Genuchten (1984), Flux-averaged and volume-averaged concentrations in continuum approaches to solute transport, *Water Resour. Res.*, *20*, 866–872.

Pedretti, D., and D. Fernàndez-Garcia (2013), A locally-adaptive and automatic method to estimate heavily-tailed breakthrough curves from particle distributions, *Adv. Water Resour.*, *59*, 52–65, doi:10.1016/j.advwatres.2013.05.006.

Pedretti, D., and A. Fiori (2013), Travel times distribution under convergent radial flow in heterogeneous formations: Insight from an exact stratified model, *Adv. Water Resour.*, *60*, 100–109, doi:10.1016/j.advwatres.2013.07.013.

Pedretti, D., D. Fernàndez-Garcia, D. Bolster, and X. Sanchez-Vila (2013), On the formation of heavy-tailed breakthrough curves during convergent flow tracer tests in three-dimensional heterogeneous sandy aquifers, *Water Resour. Res.*, *49*, 4157–4173, doi:10.1002/wrcr.20330.

Ptak, T., M. Piepenbrink, and E. Martac (2004), Tracer tests for the investigation of heterogeneous porous media and stochastic modelling of flow and transport—A review of some recent developments, *J. Hydrol.*, *294*, 122–163.

Renard, P., and D. Allard (2013), Connectivity metrics for subsurface flow and transport, *Adv. Water Resour.*, *51*, 168–196, doi:10.1016/j.advwatres.2011.12.001.

Riva, M., A. Guadagnini, D. Fernàndez-Garcia, X. Sanchez-Vila, and T. Ptak (2008), Relative importance of geostatistical and transport models in describing heavily tailed breakthrough curves at the Lauswiesen site, *J. Contam. Hydrol.*, *101*, 1–13, doi:10.1016/j.jconhyd.2008.07.004.

Rubin, Y. (2003), *Applied Stochastic Hydrogeology*, Oxford Univ. Press, N. Y.

Rubin, Y., M. A. Cushey, and A. Wilson (1997), The moments of the breakthrough curves of instantaneously and kinetically sorbing solutes in heterogeneous geologic media: Prediction and parameter inference from field measurements, *Water Resour. Res.*, *33*, 2465–2481, doi:10.1029/97WR01229.

Salamon, P., D. Fernàndez-Garcia, and J. Gomez-Hernandez (2007), Modeling tracer transport at the MADE site: The importance of heterogeneity, *Water Resour. Res.*, *43*, W08404, doi:10.1029/2006WR005522.

Sanchez-Vila, X., and J. Carrera (1997), Directional effects on convergent flow tracer tests, *Math. Geol.*, *29*(4), 551–569, doi:10.1007/BF02775086.

Sanchez-Vila, X., J. Carrera, and J. Girardi (1996), Scale effects in transmissivity, *J. Hydrol.*, *183*(1–2), 1–22.

Sharifi Haddad, A., H. Hassanzadehm, and J. Abedi (2012), Advective-diffusive mass transfer in fractured porous media with variable rock matrix block size, *J. Contam. Hydrol.*, *113*, 94–107, doi:10.1016/j.jconhyd.2012.02.008.

PEDRETTI ET AL.

1223

Silva, O., J. Carrera, M. Dentz, S. Kumar, A. Alcolea, and M. Willmann (2009), A general real-time formulation for multi-rate mass transfer problems, *Hydrol. Earth Syst. Sci.*, *13*, 1399–1411, doi:10.5194/hess-13-1399-2009.

Trinchero, P., X. Sanchez-Vila, and D. Fernàndez-Garcia (2008), Point-to-point connectivity, an abstract concept or a key issue for risk assessment studies?, *Adv. Water Resour.*, *31*(12), 1742–1753, doi:10.1016/j.advwatres.2008.09.001.

Valocchi, A. J. (1985), Validity of the local equilibrium assumption for modeling sorbing solute transport through homogeneous soils, *Water Resour. Res.*, *21*, 808–820.

Willmann, M., J. Carrera, and X. Sanchez-Vila (2008), Transport upscaling in heterogeneous aquifers: What physical parameters control memory functions?, *Water Resour. Res.*, *44*, W12437, doi:10.1029/2007WR006531.

Willmann, M., J. Carrera, X. Sanchez-Vila, O. Silva, and M. Dentz (2010), Coupling of mass transfer and reactive transport for nonlinear reactions in heterogeneous media, *Water Resour. Res.*, *46*, W07512, doi:10.1029/2009WR007739.

Zhang, Y., D. A. Benson, and B. Baeumer (2007), Predicting the tails of breakthrough curves in regional-scale alluvial systems, *Ground Water*, *45*(4), 473–484, doi:10.1111/j.1745-6584.2007.00320.x.

Zinn, B., and C. F. Harvey (2003), When good statistical models of aquifer heterogeneity go bad: A comparison of flow, dispersion and mass transfer in connected and multivariate Gaussian hydraulic conductivity fields, *Water Resour. Res.*, *39*(3), 1051, doi:10.1029/2001WR001146.

Zinn, B., L. C. Meigs, C. F. Harvey, R. Haggerty, W. J. Peplinski, and C. Freiherr von Schwerin (2004), Experimental visualization of solute transport and mass transfer processes in two-dimensional conductivity fields with connected regions of high conductivity, *Environ. Sci. Technol.*, *38*(14), 3916–3926, doi:10.1021/es034958g.